International Journal of Pharmaceutics 674 (2025) 125400

Contents lists available at ScienceDirect

International Journal of Pharmaceutics

journal homepage: www.elsevier.com/locate/ijpharm

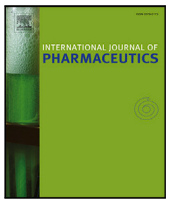

Delivery of viscous drops and jets to eyeball replicas

Idera Lawal[1,2], Pankaj Rohilla[1,3], Eliana Rodriguez, Phuong Pham, Jeremy Marston *

Department of Chemical Engineering, Texas Tech University, Lubbock, TX 79409, United States of America

ARTICLE INFO

Keywords:
Drop impact
Jet impact
Ophthalmic
Viscosity

ABSTRACT

Front-of-the-eye (FOTE) droplet-based drug delivery presents a challenging fluid dynamics phenomenon, where many patients either miss their target or blink prematurely, leading to significant drug wastage and poor bioavailability. In this study, we investigate the influence of fluid properties and impact speed on the impact-spreading process on eyeball replica substrates in the context of both drops and jets to identify optimal parameters for maximum spreading, which has implications for bioavailability. Additionally, we investigate the role of the micro-scale protective tear film by coating the substrates with artificial tears. Our findings reveal that the presence of a tear film enhances the spreading of eye drops, and the spreading dynamics of various Newtonian and non-Newtonian fluids on both dry and wet substrates can be described by a universal scaling law.

1. Introduction

The treatment of common eye disorders such as ocular hypertension, bulging eyes, diabetic macular edema, and glaucoma can involve medication delivery using various methods (Rupenthal and Audghtery, 2019; Winfield et al., 1990; Sultana et al., 2007; Noymer et al., 2019; Yellepeddi and Palakurthi, 2016) such as front-of-the-eye (FOTE), back-of-the-eye (BOTE), and intraocular. Of these, FOTE delivery is the most common with analyses indicating that it accounts for nearly 90% of the market where 62% of medications are delivered from standard dropper bottles (Zielinski and Sullivan, 2007; Patel et al., 2013).

However, FOTE delivery, typically administered via eye drops, presents several challenges such as the blink reflex (≤100 ms), spilling, drainage to the tear ducts, and improper administration technique, resulting in nearly 80% of every single droplet being wasted (Jumelle et al., 2020; St. Peter et al., 2023).

The standard process entails the release of a discrete droplet (20-60 μl) of medicated solution using a dropper bottle with the aim of impacting the cornea and remaining there long enough for the drug to interact. To this end, polymers are frequently added as viscosity modifiers to improve adhesion, yielding both viscous and non-Newtonian solutions, yet the role of rheological properties has not been extensively studied in FOTE delivery. Understanding the underlying mechanisms for liquid spreading on eyeballs can help guide designs of new devices for FOTE delivery to address ineffective administration and drug wastage. Of particular note are two novel approaches that involve the use of small-volume droplets (Sullivan and Nelson, 2010) or jets (Quiroz-Mercado et al., 2020) fired onto the cornea.

In light of these factors, we herein study the impact and spreading dynamics of droplets and jets, with an emphasis on elucidating the role of fluid properties, impact speed, and the presence of an existing tear film.

2. Theory of spreading dyanmics

Drop impact dynamics have been extensively studied and in this section we present only a brief overview of the salient modeling efforts, whilst for comprehensive reviews we refer the reader to Yarin (2006), Josserand and Thoroddsen (2016), Cheng et al. (2022). The typical outcomes of drop impact are: spreading, receding, splashing, and bouncing, which are governed by several parameters, including droplet diameter (D_0), impact velocity (U_0), fluid properties (e.g., viscosity μ, surface tension σ, and density ρ), and substrate topography and chemistry. The majority of prior studies have been performed with flat substrates (Bakshi et al., 2007; Rioboo et al., 2002), but several studies for curved substrates have also been reported (Long et al., 2022; Liang et al., 2013, 2014; Chen and Bertola, 2017).

In the initial stages, the impacting droplet morphs into the shape of a truncated sphere, followed by the formation of a rim called the lamella, as the leading edge spreads radially outward from the axis of

* Corresponding author.
E-mail address: jeremy.marston@ttu.edu (J. Marston).
[1] Equal contribution.
[2] Present affiliation: Procept Biorobotics, 150 Baytech Dr., San Jose, CA 95134.
[3] Present affiliation: School of Chemical and Biomolecular Engineering, Georgia Institute of Technology.

https://doi.org/10.1016/j.ijpharm.2025.125400
Received 10 January 2025; Received in revised form 18 February 2025; Accepted 22 February 2025
Available online 5 March 2025

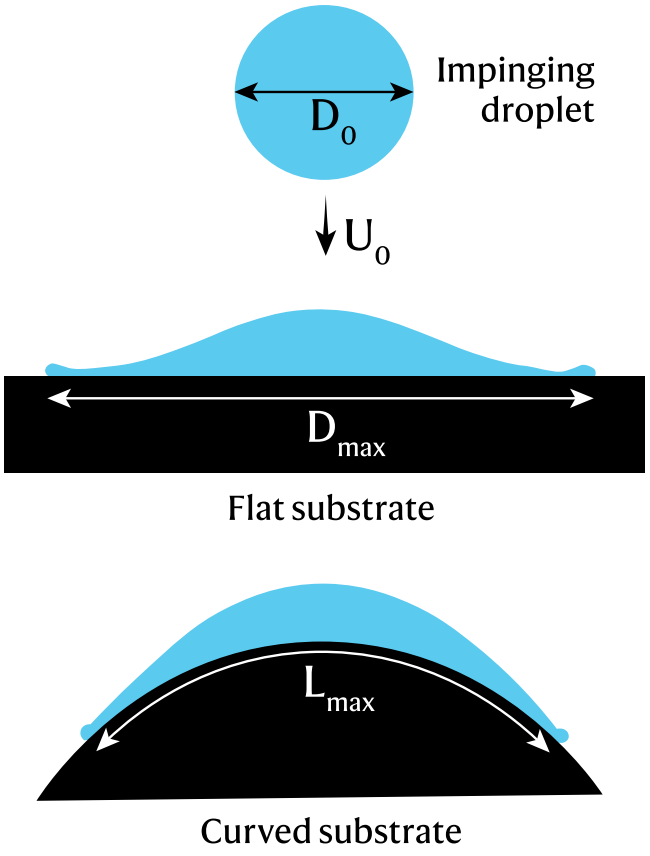

Fig. 1. Maximum spread on flat (D_{max}) and curved (L_{max}) substrates.

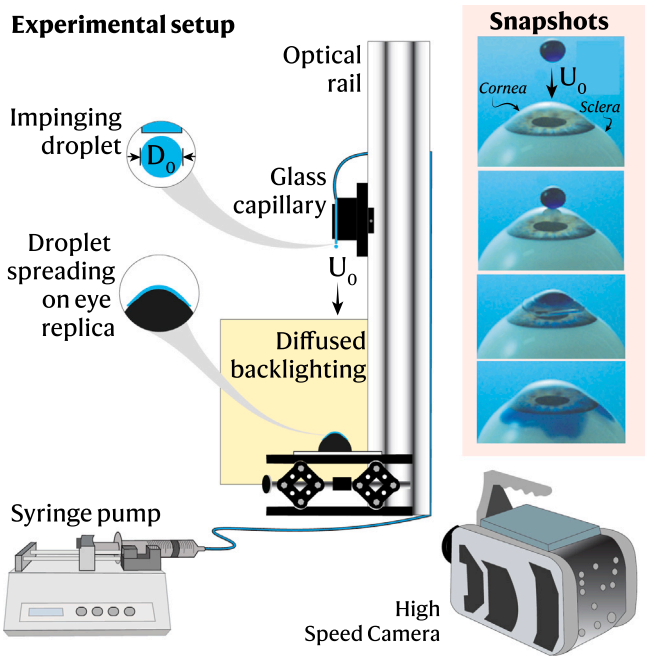

Fig. 2. Experimental setup and example impact sequence of a 3.9 mm water droplet.

symmetry. The early-time dynamics of the droplet are dictated by competition between the kinetic and surface energy of the fluid, whilst the maximum spreading length (D_{max} or L_{max}, see Fig. 1) of the fluid over the substrate is typically described by energy conservation models that also consider viscous dissipation. After the maximum spread has been reached, the droplet may retract under surface tension and undergo rebound or oscillations until a final spread (L_f) has been reached. In the context of FOTE droplet delivery, the final spread length (L_f) dictates the thickness of the film and area of the eyeball covered with drug, thus influencing the bioavailability of the drug.

For inviscid conditions, complete conversion of kinetic energy to surface energy yields scalings in terms of the impact Weber number, $\beta_{max} \sim We^{\alpha_1}$, where $\beta_{max} = L_{max}/D_0$, $We = \rho U_0^2 D_0/\sigma$, and $\alpha_1 = 1/4, 1/2$ based on either energy or momentum conservation and the effective deceleration (Bennett and Poulikakos, 1993; Clanet et al., 2004). On the other hand, the assumption of complete dissipation of kinetic energy of the droplet at the maximum spread yields scalings in the viscous regime, $\beta_{max} \sim Re^{\alpha_2}$, where $Re = \rho D_0 U_0/\mu$, and $\alpha_2 = 1/5, 1/4$ from theory and experimental studies, respectively (Chandra and Avedisian, 1991; Clanet et al., 2004). To account for both viscosity and capillarity, interpolations between the inviscid and viscous regimes have led to models of the form $\beta_{max} \propto Re^{1/5} f_{EC}(We.Re^{-2/5})$ (for energy conservation) (Eggers et al., 2010), and $\beta_{max} \propto Re^{1/5} f_{MC}(We.Re^{-4/5})$ (from momentum conservation) (Clanet et al., 2004); here, f_{EC} and f_{MC} are the functions for the energy-conservation and momentum conservation models, respectively, which are to be determined empirically. One approach that seeks to provide the best functional description across a broad range of We and Re numbers is found in Laan et al. (2014), where they used a Padé approximant $\beta_{max} Re^{-1/5} = P_1^{1/2}/(A + P_1^{1/2})$ with $P_1 = We Re^{-2/5}$.

Although several scaling correlations have been proposed for maximal spreading over curved substrates (Yoon and Shin, 2021; Liu et al., 2019; Khurana et al., 2019), both curvatures of the eye (cornea, $R \sim$ 6 mm, and sclera, $R \sim$ 12 mm) are 3–8 times larger than the droplet size, suggesting the scalings for flat surfaces may be applicable. In addition, the impact-spreading process for pre-wetted curved substrates, as is the case for eyeballs due to the tear film, has not been studied as extensively, with the exceptions of Liang et al. (2013, 2014). Moreover, to our knowledge, none of the published reports investigate the volumes, curvatures, and fluid properties that specifically match those that are relevant for FOTE application.

As such, we herein investigate the role of fluid rheology, impact speed, and the presence of liquid film on the outcome of spreading dynamics over substrates mimicking the human eye, using the established scaling approaches to provide the best functional descriptions of our data. Furthermore, in light of recent device development (Quiroz-Mercado et al., 2020), we also explore the dynamics of jet-based delivery.

3. Methods

Experimental Setup: The schematic representation of the experimental setup is shown in Fig. 2. The droplets were generated using a low flow syringe pump, a 5 ml syringe, and flexible tubing attached to a glass capillary with a tapered hydrophobized orifice. This arrangement yielded a reproducible drop release and diameter, $D_0 \approx 3-4$ mm (Vol $\approx 14-34$ μL). The height, h, of the glass capillary above the target was varied to increase the impact speed, $U_0 \approx \sqrt{2gh} \approx 0.5-2$ m/s. Discrete jets were generated via spark-induced jetting from a transparent polycarbonate tube (inner dia = 3.2 mm and outer dia = 6.3 mm). The spacing between the fluid meniscus in the glass capillary and the eyeball replica was kept at 6 mm. The methodology and details of the device used to generate discrete liquid jets are described in Rohilla and Marston (2023).

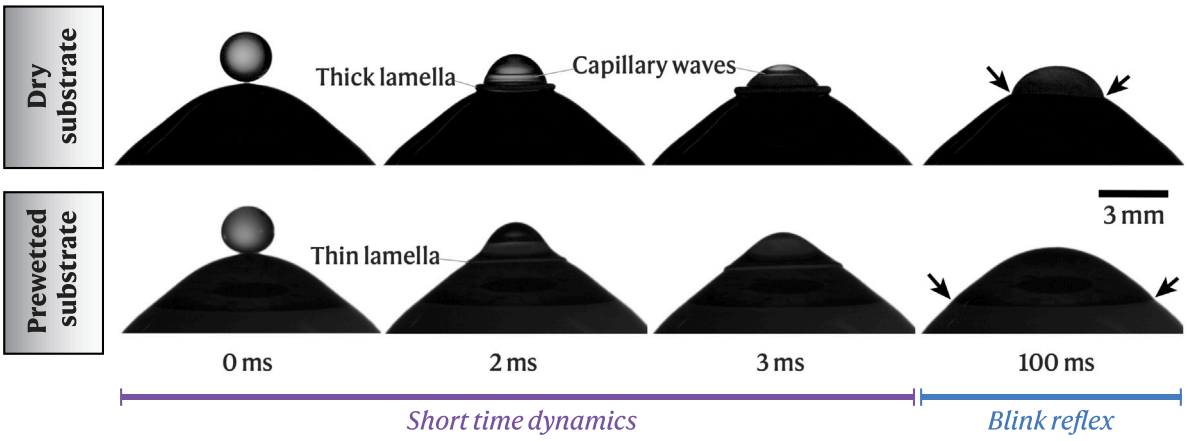

Fig. 3. Example impact sequences to highlight the difference between dry (top row) and pre-wet (bottom row) targets. In both cases, the drop is water, with U_0 = 1.25 m/s, yielding $Re = 3743$ and $We = 64$.

Table 1
Physical properties of the fluids used. μ for non-Newtonian fluids corresponds to apparent viscosity for $\dot{\gamma} \sim 125 - 667$ s^{-1}. Aqueous solution concentrations are in $\%_{w/w}$.

Fluid	μ (mPa s)	ρ (kg/m^3)	σ (mN/m)
DI water	1	998	72.8
50% glycerol[a]	7	1130	70
60% glycerol	13.7	1156	66.68
80% glycerol	84	1209	64.66
0.125% CMC	55–71	1004	68
0.25% CMC	64–89	1006	68
C.E.L.	26–28	1003	53.56

[a] 50% glycerol solution was only used for viscous jetting.

The target substrates used herein were either spheres or acrylic eyeball replicas, where the spheres were used as a control to understand the effect of the double curvature of the eyeballs. Furthermore, to understand the role of the tear film, the targets were pre-wetted with a commercial artificial tears eye lubricant (C.E.L.) solution (CVS Health). After applying several droplets of solution to the target, the residual film was estimated to be approximately 5-10 μm thick using high-resolution imaging and background subtraction.

Imaging: High-speed cameras (e.g. Phantom V711, Vision Research Inc.) were used to record the impact with a typical frame rate of 10,000 fps and exposure times of 50 μs. Using Nikon micro-Nikkor lenses, we achieved an effective pixel size of ~ 41 μm/px. The videos were processed using a custom MATLAB script that employed binarization, background subtraction, and tracked the edges of the spreading droplet, yielding time-resolved spreading information from which we could identify the impact speed, and the maximum and final spread diameters. To ensure precise droplet impact at the apex of the target substrate, we carefully analyzed the high-speed videos recorded from orthogonally positioned cameras.

Fluid Properties: Fluid viscosity was varied by using DI water, water-glycerol mixtures (60%$_{w/w}$ and 80%$_{w/w}$), and weak polymeric solutions of carboxymethyl cellulose (CMC with concentrations of 0.0625%$_{w/w}$, 0.125%$_{w/w}$ and 0.25%$_{w/w}$ in water). The effective viscosity of the CMC solutions was estimated from the rheological profiles (measured with DHR 2.0 rheometer, TA Instruments) and characteristic shear rates from the impact event ($\dot{\gamma} \sim U_0/D_0 \approx 125 - 667$ s^{-1}, see fig. S2). The surface tension of the fluids was measured using the pendant drop technique using the ImageJ plugin for pendant drop (Daerr and Mogne, 2016). The physical properties of the fluids used in this study are presented in Table 1.

4. Results

4.1. Droplet delivery to the FOTE

Overview of dynamics. Fig. 3 shows impact sequences for both dry and pre-wet eyeball targets with water droplets, with frames taken directly from the high-speed video. The droplet diameter here is $D_0 \approx$ 3 mm, yielding a delivery volume of ≈ 14 μL. The early dynamics are represented by the first 3 images up to t = 3 ms, whilst the final image represents the approximate onset of the blink reflex at t = 100 ms. The principal differences between the dry and wet impacts are manifested by (i) the increased thickness of the rim (lamella) for the dry target, and (ii) the reduced spread for the dry target compared to the pre-wet case. As noted by the arrows in the final image marking the location of the edge of the spread, we observe that the drop spreads significantly farther on the pre-wet target, reaching past the cornea and on to the sclera; whereas the droplet on the dry target is arrested on the cornea.

For a more comprehensive overview of the effects of pre-wetting and the double curvature, Fig. 4(a) shows comparisons between both spheres and eyeball replicas at different impact speeds. Focusing first on the dry targets, we observe that the maximum spread is attained at approximately the same time on both the spherical and eyeball targets, but that the increased curvature of the cornea results in a slight increase in spread for the eyeball replicas, as seen in Fig. 4(b) (and the SI Video). As the impact speed is increased from 0.5 to 2 m/s, the spread increases significantly from $\beta_{max} \approx 1.70 \rightarrow 4.2$, which can be seen in both the spherical and eyeball targets. In all cases for the dry substrates, the drops then retract from the maximum spread to reach their equilibrium (final spread, D_f) within approximately 50 ms (see Fig. 4(b)), ahead of t_{BR} = 100 ms. Note that for U_0 = 2 m/s, the maximum spread coincides with the formation of a notably thicker rim at the leading edge, due to a confluence of fluid momentum 'draining' fluid away from the apex to the leading edge and surface tension forces acting to restore the drop toward an equilibrium.

The cases where the targets are pre-wet with the artificial tears present a qualitative shift in dynamics; First, even for the low impact speeds at the intermediate times of 11.83 and 12.33 ms, respectively, we observe a considerable increase in spread, without a pronounced local maxima — here the fluid from the droplet simply continues to merge with existing film until t_{BR}. For the higher impact speeds,

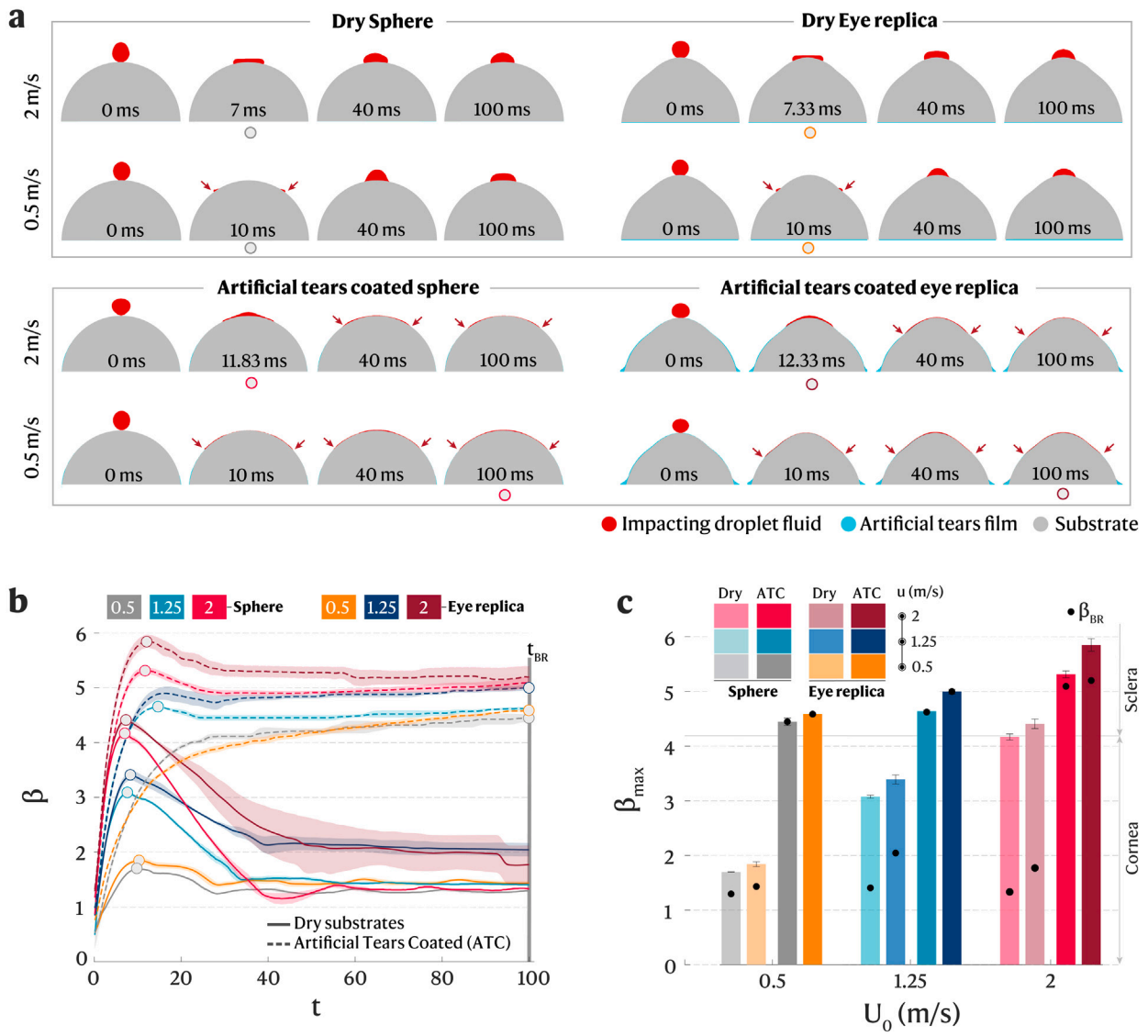

Fig. 4. (a) Snapshots of processed images for water droplets impacting onto dry and pre-wetted spheres and eyeball replicas. Gray represents the solid substrate, cyan the artificial tears film, and red is the droplet. The red arrows indicate the extent of spreading, and the circles below the images mark the maximum spread; (b) Time-resolved dimensionless spread $\beta = L(t)/D_0$, with circles marking β_{max}; (c) Maximum spread for the different conditions in (b), with the black dots marking the point when t_{BR} occurs.

the maximum spread is attained at around 10 ms, but there is no pronounced retraction, and no thickened rim at the leading edge, as the fluid from the droplet becomes incorporated into the existing film. Although the fluid from the droplets would continue to merge and drain under gravity, we only consider dynamics up to the blink reflex, $t_{BR} \approx 100$ ms (as in Fig. 4(b)). Lastly, in Fig. 4(c), we indicate which of these cases would completely coat the cornea and reach the sclera, which is indicated by trial surpassing the solid gray line at $\beta_{max} \approx 4.2$ (or ≈ 16.8 mm for water). We find that all the pre-wet cases reach the sclera at t_{BR}, whilst none of the dry surface cases do.

In summary, we observe that both increasing impact speed and the presence of a pre-existing coating significantly enhance the maximum spread. However, the final spread that is attained at the time of the blink, i.e. $\beta(t = t_{BR})$, is less dependent on impact speed, and shape of the target, and is dictated by the presence of the artificial tears coating. We can estimate the final thickness of the fluid film from volume conservation between the impacting droplet of diameter, D_0, and the final spread at the blink reflex, D_{BR}, as $h \approx (2D_0)/(3\beta_{BR}^2)$. For example, a 4-mm water droplet on a dry eyeball has $\beta_{BR} \approx 1.5 - 2$, which yields $h = 0.67 - 1.18$ mm, whereas the pre-wetted eyeball has $\beta_{BR} \approx 4.5 - 5.2$, yielding $h \approx 98 - 107$ μm. As such, the experiments onto pre-wetted eyeball replicas indicate that a thin film of fluid would be achieved within the blink reflex time, and that the coverage extends past the cornea.

A more granular analysis of the effect of impact speed and pre-wetting is presented in Fig. 5, showing a range of impact speeds from $U_0 = 0.5 - 2$ m/s for both dry and wet eyeballs. The increased inertia always leads to increased maximum spread (typically occurring around $t \approx 5 - 10$ ms), but the final spread is virtually independent of impact speed, and all the curves for dry targets converge to a constant spread of 6–7 mm. The same phenomena (i.e., independence of impact speed) is noted for pre-wet targets, albeit the spread length is significantly higher at around 24 mm and continuing to increase (note that all curves are still sloping upward even for $t > t_{BR}$).

Viscous drops and universal scaling. Increasing the fluid viscosity, decreased the spread on both dry and pre-wetted eyeballs, as observed

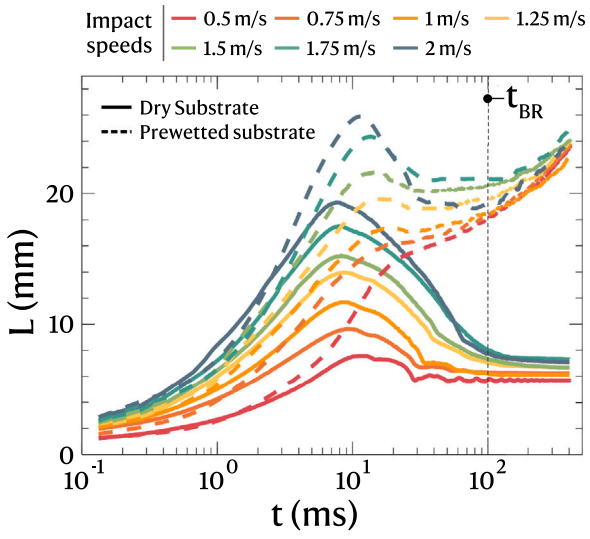

Fig. 5. Spreading dynamics for water droplets on dry (solid lines) and pre-wet (dashed lines) eyeball replicas. The impact speeds range from 0.5–2 m/s (Re = 2000 – 8000, We = 13 – 213). The vertical dashed line indicates the blink reflex time.

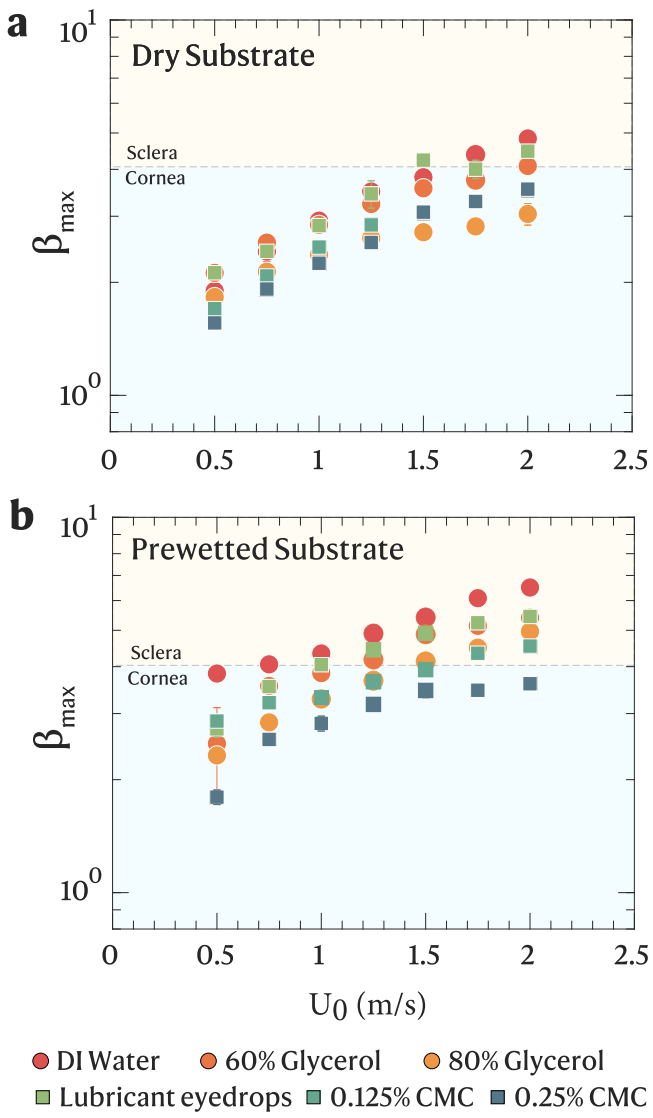

Fig. 6. Maximum spreading length of droplets of different fluids impacting eyeball replica at different impact speeds. Data points represent the mean values, with error bars indicating the standard deviation (n=4).

in Fig. 6. Here, the aggregate data across all viscosities and impact speeds shows that the largest spread occurs for the lowest viscosities and highest impact speeds, corresponding to the largest Reynolds number, as expected from prior literature relations such as $\beta_{max} \sim Re^{\alpha_2}$ (Clanet et al., 2004; Chandra and Avedisian, 1991). The strictly Newtonian fluids – namely – water, 60% and 80% glycerol follow expected trends with decreased spread as the viscosity increases at any given impact speed. Intuitively, we expect non-Newtonian fluids (C.E.L, and CMC solutions) to be nuanced by the change in apparent viscosity, μ_a, which depends on the shear rate. Here, we use the estimate $\dot{\gamma} \sim U_0/D_0$ as the characteristic shear rate for the impact, although the value is highly variable through the droplet at different stages of impact. Nonetheless, the initial impact shear rate would imply that higher impact speeds lead to higher shear rates, and thus lower apparent viscosities and higher spreading. However, this does not manifest in the data, and we observe that the trends for the non-Newtonian solutions generally follow those for the Newtonian fluids. As such, we can characterize the full range of fluids with their Newtonian or apparent viscosities, which enables us to seek a universal scaling relations for our data.

Following the preceding literature, we tested simple scaling approaches using We^{α_1} and Re^{α_2}; however, both failed to collapse the data (see fig. S3 and S4). The energy conservation approach, i.e., $\beta_{max} Re^{-1/5} = P_1^{1/2}/(A + P_1^{1/2})$, with the impact parameter $P_1 = WeRe^{-2/5}$, resulted in the best data collapse compared to the momentum conservation approach with the impact parameter $P_2 = WeRe^{-4/5}$ (see fig. S5). This fitting is shown in Fig. 7 for (a) dry and (b) pre-wet, with corresponding coefficients of determination of $R^2 = 0.68$ and 0.56, respectively. The lower R^2 value for the impact onto the pre-wetted targets indicates that more variation in the data must be attributed to other sources which, for this experiment, are likely to be the effects of the film and the double curvature. Nonetheless, this scaling approach provides a reasonable collapse of data across a range of viscosities and impact speeds that may be encountered in real-life eye drop applications.

4.2. Jet delivery to the FOTE

Delivering medication in the form of a fluid stream to the front of the eye has been observed to be an effective alternative to the traditional dropper method, while offering improved drug exposure and better comfort during administration (Noymer et al., 2019; Quiroz-Mercado et al., 2020). Guided by these reports, we studied the delivery of discrete viscous jets to the eyeball replicas. In this study, we used a custom-built electric discharge device to generate spark-induced discrete liquid jets with varying viscosities. Fig. 8a shows the RC circuit used in the jetting device (Rohilla and Marston, 2023). The jetting mechanism involves creation of a cavitation bubble due to instant vaporization of fluid caused by an electrical discharge at a specific point within the fluid-filled capillary tube (see Fig. 8b). The resulting cavitation bubble expands rapidly, expelling the fluid as a discrete, focused jet. Liquid jets of varying viscosity were directed to impinge at the front of the eyeball replica. The comparative spreading dynamics of discrete liquid jets of 50% and 60% glycerol solutions on an eyeball replica is presented in Fig. 8c–f.

Jet characterization. A discharge voltage of 30 V generated viscous jets of 50%, 60% and 80% glycerol solutions with comparable maximum jet tip speeds (U_j) of ~ 20 ± 4.5 m/s, ~ 20 ± 4.3 m/s, and

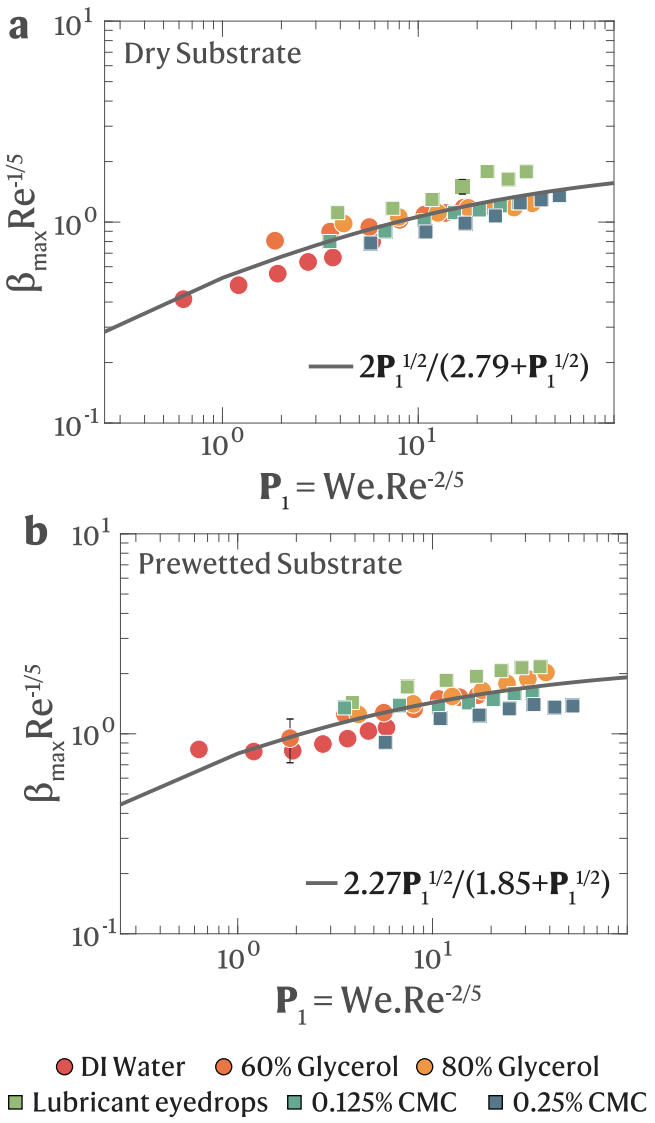

Fig. 7. Scaled spreading lengths of droplets of all viscosities and impact speeds plotted in terms of the impact parameter, $P_1 = WeRe^{-2/5}$, based on energy conservation; (a) dry eyeball replica, and (b) pre-wetted eyeball replica. Error bars represent standard deviation (n=4).

$\sim$ 21.4 m/s, respectively. For these viscous jets, high Weber numbers ($We_j = \rho U_j^2 d_j/\sigma \gtrsim 3000$) indicated that the inertial forces dominated the surface tension forces.

A higher discharge voltage of 45 V produced faster and turbulent jets. The jet speeds of 50%, 60%, and 80% glycerol for a discharge voltage of 45 V were 35.15 ± 6.4 m/s, 36.4 ± 1.3 ms, and 41 ± 3.8 ms respectively. Weber numbers for these fluids were $\sim O(10^4)$, leading to higher propensity for splashing.

Spreading behavior. The spreading behavior of the 60% glycerol jet streams impacting the dry eyeball replica were qualitatively similar to impinging droplets, characterized by a distinct rim at the leading edge, maximum spread, and a final shape resembling a spherical cap (see Fig. 8c). Similar to droplets impacting pre-wetted substrates, jets of 60% glycerol (30 V) exhibited larger spreading on eyeball replicas coated with artificial tear film compared to dry substrates. Additionally, 60% glycerol jet (30 V) impacting pre-wetted eyeball replica produced a distinctive splash-crown (t = 0.33 ms, Fig. 8d, also see the SI video). Jets of 50% glycerol (30 V) spread farther on dry substrates than 60% glycerol jets (Fig. 8e). However, these lower-viscosity jets also resulted in splash back from the eyeball replica surface (Fig. 8f), rendering them undesirable for FOTE delivery applications. Such splashing in jets could be attributed to their higher inertial forces ($We_j \gg We_{drop}$) overcoming the opposing forces such as capillary pressure and viscous stress.

We quantified the spreading dynamics of viscous jets on prewetted eyeball replicas (Fig. 9a–b) as follows; As the stand-off distance between the meniscus and the substrate, $H_{M\text{-}S}$, increased from 6 to 15 mm, the maximal spreading length for 50% glycerol jets grew from approximately 5 mm to 9.2 mm, while for 60% glycerol, it increased non-linearly from around 5 mm to 9.9 mm. 80% glycerol jets exhibited lower spreading lengths of 4.15 mm and 8.27 mm at $H_{M\text{-}S}$ = 6 mm and 15 mm, respectively, with a slightly higher value (8.5 mm) observed at $H_{M\text{-}S}$ = 12 mm. The large variations in spreading length were likely due to splashing and misalignment between the jet tip and the target center, or from asymmetrical collapse of the cavitation bubble, pulling the jet to one side, which would be exaggerated at increased heights.

Discharge voltages below 30 V did not generate liquid jets (Rohilla and Marston, 2023), therefore only a specific range of voltages can be used for spark-induced jetting to be a viable delivery technique. This caveat notwithstanding, the deposited volumes with this technique are in the range of $\sim 3-15$ μL, which means it could be fine-tuned for FOTE delivery. It is important to note that spark-induced jets may degrade the drug or introduce brass particles from the electrodes into the drug, which is undesirable. To address this, further exploration of designs incorporating separate chambers for the spark and drug storage, separated by a flexible membrane (Han and Yoh, 2010), could help preserve drug integrity during the jetting process. Furthermore, alternative techniques for generating discrete jets, such as piezoelectric mechanisms (Stachowiak et al., 2007) or laser-induced thermocavitation (Tagawa et al., 2012), could also be used for applications in FOTE, which could potentially mitigate the issue of brass electrode degradation.

5. Conclusions

Self-administration of eyedrops by patients often leads to varying results due to misalignment of the dropper bottle, and various heights above the eye. Furthermore, significant wastage can occur due to excess droplet volume and drainage from low-viscosity products. To address these issues, novel devices seek to deliver products with viscosity modifiers and small volumes by impacting a single droplet (or discrete jet) onto the eyeball.

To study these processes we conducted an experimental investigation of impact on eyeball replicas with and without a coating of artificial tears to simulate events for FOTE fluid delivery. Our range of fluids was representative of commercially available eye drop solutions (~1 – 70 mPa s) (Doshi and Xu, 2009).

There are significant differences between impact events for dry and pre-wet eyeball targets, whereby droplets on pre-wet targets experience a much enhanced spreading. In addition, a comparison between a simple sphere and the eyeball replicas showed that the double curvature of the eyeball assists the spreading, but to a lesser extent than the tear film.

Our study suggests that for eye drops with water-like viscosity, a low impact speed of 0.5 m/s is sufficient to achieve complete coverage across the cornea and onto the sclera, whilst for dry surfaces (e.g., dry eye syndrome), higher impact speeds of $\sim$ 1.75 m/s are needed for the same coverage. For fluids with viscosity above $\sim$ 10 mPa.s onto dry targets, even the highest speeds of 2 m/s were insufficient to cover the cornea; however, for the pre-wet targets, speeds above 1.5 m/s were generally sufficient to achieve complete coverage. Even for fluids with viscosity up to 80 cP, once the impact speed exceeds 1.5 m/s, the spreading extends to the sclera within the blink reflex timescale.

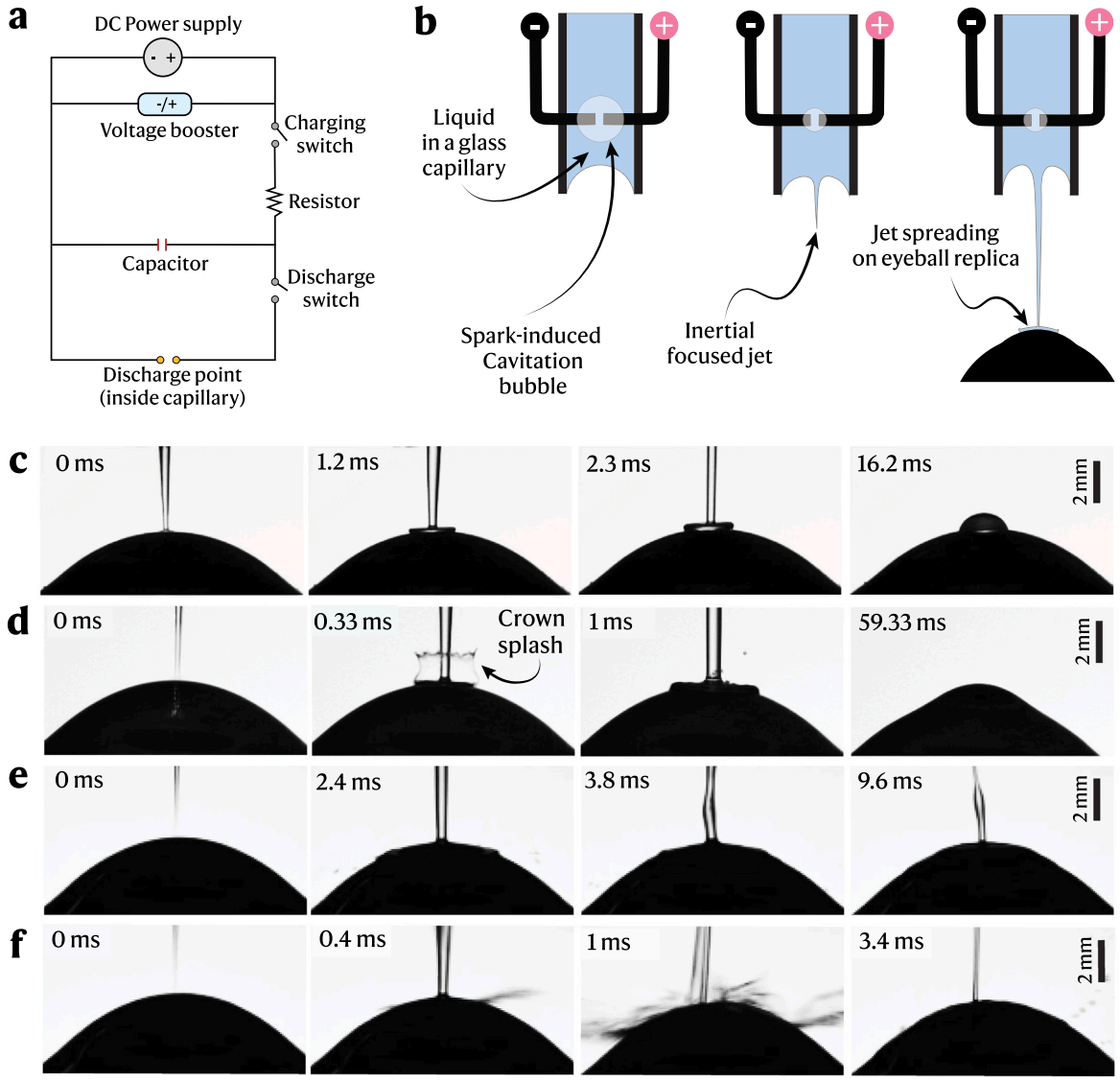

Fig. 8. Delivering viscous jets to eyeball replica. (a) an RC circuit used in the spark-induced jetting device. (b) Illustration showing the sequence of jetting mechanism induced by spark-induced cavitation. Snapshot sequences of 60% liquid jets impinging and spreading onto (c) dry and (d) pre-wetted eyeball replicas (discharge voltage = 30 V). Panels (e) and (f) show snapshots of 50% glycerol jets generated at discharge voltages of 30 V and 45 V, respectively, as they impinge and spread on prewetted substrates. In all cases (c–f), $H_{M\text{-}S}$ was maintained at 6 mm.

Spreading beyond the cornea renders a thin coating (~100 μm) which is less prone to being squeezed out by the eyelids during the blink.

Viscous jets exhibited lower spreading lengths than droplets primarily due to differences in delivery volume. While their spreading dynamics on dry substrates were qualitatively similar, viscous jets showed significant variations in spreading length at higher $H_{M\text{-}S}$ due to splashing caused by increased impact speeds. Since splashing is undesirable for FOTE drug delivery, these findings highlight the need for enhanced control and precision in this technique.

Some limitations of the present study are: (1) the pre-existing film implemented by adding a few drops of artificial tears was not of uniform thickness due to drainage under gravity, nor was it the same fluid as the drops (except for the CEL drops); (2) the drop diameters varied slightly from fluid to fluid due to the effect of physical properties; (3) we did not account for dynamic shear-thinning effects, only an effective viscosity based on a characteristic shear rate. Despite these limitations, our data was reasonably well described by previously reported non-dimensional relations in terms of the impact Weber and Reynolds numbers, providing an initial framework for manufacturers seeking to develop devices for FOTE drug delivery of viscous products.

CRediT authorship contribution statement

Idera Lawal: Writing – original draft, Formal analysis, Data curation. **Pankaj Rohilla:** Writing – review & editing, Writing – original draft, Formal analysis, Data curation. **Eliana Rodriguez:** Data curation. **Phuong Pham:** Data curation. **Jeremy Marston:** Writing – review & editing, Project administration, Methodology, Funding acquisition, Conceptualization.

Declaration of competing interest

The authors of this work declare no competing interests.

Acknowledgment

This work was initiated under financial support from The National Science Foundation via award CBET-1749382, awarded to J.M.

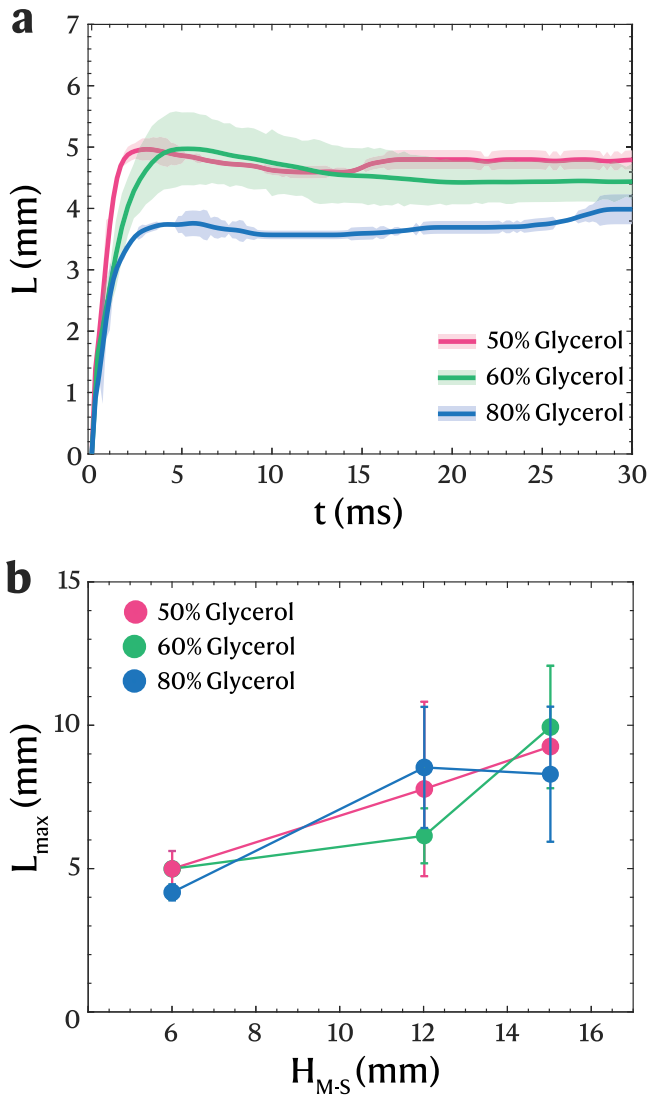

Fig. 9. Spreading dynamics of viscous jets on a prewetted eyeball replica at a discharge voltage of 30 V. (a) Temporal evolution of spreading length for viscous jets on the eyeball replica. Solid lines indicate the mean spreading length over time, with shaded regions representing the standard deviation ($H_{M\text{-}S}$ = 6 mm, n = 3). (b) Maximum spreading length achieved by viscous jets as a function of $H_{M\text{-}S}$ and fluid viscosity (n = 3).

Appendix A. Supplementary data

Supplementary material related to this article can be found online at https://doi.org/10.1016/j.ijpharm.2025.125400.

Data availability

Data will be made available on request.

References

Bakshi, Shamit, Roisman, Ilia V., Tropea, Cam, 2007. Investigations on the impact of a drop onto a small spherical target. Phys. Fluids 19 (3), 032102.
Bennett, T., Poulikakos, D., 1993. Splat-quench solidification: estimating the maximum spreading of a droplet impacting a solid surface. J. Mater. Sci. 28, 963–970.
Chandra, S., Avedisian, C.T., 1991. On the collision of a droplet with a solid surface. Proc. R. Soc. Lond. Ser. A: Math. Phys. Sci. 432 (1884), 13–41.
Chen, Simeng, Bertola, Volfango, 2017. Drop impact on spherical soft surfaces. Phys. Fluids 29 (8), 082106.
Cheng, X., Sun, T.-P., Gordillo, L., 2022. Drop impact dynamics: Impact force and stress. Annu. Rev. Fluid Mech. 54, 57–81.
Clanet, Christophe, Béguin, Cédric, Richard, Denis, Quéré, David, 2004. Maximal deformation of an impacting drop. J. Fluid Mech. 517, 199–208.
Daerr, Adrian, Mogne, Adrien, 2016. Pendent_drop: an imagej plugin to measure the surface tension from an image of a pendent drop. J. Open Res. Softw. 4 (1), e3.
Doshi, U., Xu, J., 2009. Effect of viscosity, surface tension and mucoadhesion on ocular residence time of lubricant eye drops. Investig. Ophthalmol. Vis. Sci. 50 (13), 4641.
Eggers, Jens, Fontelos, Marco A, Josserand, Christophe, Zaleski, Stéphane, 2010. Drop dynamics after impact on a solid wall: theory and simulations. Phys. Fluids 22 (6).
Han, T.-H., Yoh, J.J, 2010. A laser based reusable microjet injector for transdermal drug delivery. J. Appl. Phys. 107, 103110.
Josserand, Christophe, Thoroddsen, Sigurdur T., 2016. Drop impact on a solid surface. Annu. Rev. Fluid Mech. 48, 365–391.
Jumelle, Clotilde, Gholizadeh, Shima, Annabi, Nasim, Dana, Reza, 2020. Advances and limitations of drug delivery systems formulated as eye drops. J. Control. Release 321, 1–22.
Khurana, Gargi, Sahoo, Nilamani, Dhar, Purbarun, 2019. Phenomenology of droplet collision hydrodynamics on wetting and non-wetting spheres. Phys. Fluids 31 (7).
Laan, Nick, de Bruin, Karla G, Bartolo, Denis, Josserand, Christophe, Bonn, Daniel, 2014. Maximum diameter of impacting liquid droplets. Phys. Rev. Appl. 2 (4), 044018.
Liang, Gangtao, Guo, Yali, Mu, Xingsen, Shen, Shengqiang, 2014. Experimental investigation of a drop impacting on wetted spheres. Exp. Therm. Fluid Sci. 55, 150–157.
Liang, Gangtao, Guo, Yali, Yang, Yong, Guo, Song, Shen, Shengqiang, 2013. Special phenomena from a single liquid drop impact on wetted cylindrical surfaces. Exp. Therm. Fluid Sci. 51, 18–27.
Liu, Xin, Zhang, Xuan, Min, Jingchun, 2019. Maximum spreading of droplets impacting spherical surfaces. Phys. Fluids 31 (9).
Long, Ming, Hasanyan, Jalil, Jung, Sunghwan, 2022. Spreading dynamics of a droplet impacting a sphere. Phys. Fluids 34 (10), 102115.
Noymer, Peter, Ivri, Ehud, Quintana, Reynaldo, Blumenkranz, Mark, 2019. AcustreamTM: Bringing topical ophthalmic drug delivery into the modern era. On Drug Deliv. 94, 32–35.
Patel, A., Cholkar, K., Agrahari, V., Mitra, A.K., 2013. Ocular drug delivery systems: An overview. World J. Pharmacol. 2 (2), 47–64.
Quiroz-Mercado, H., Ivri, E., Gonzalez-Salinas, R., et al., 2020. Clinical evaluation of a novel electromechanical topical ocular drug delivery system: Two phase 1 proof of concept studies. Clin. Ophthamol. 14, 139–147.
Rioboo, R., Marengo, M., Tropea, C., 2002. Time evolution of liquid drop impact onto solid, dry surfaces. Exp. Fluids 33 (1), 112–124.
Rohilla, P., Marston, J.O., 2023. Focused, high-speed liquid jets induced via low-voltage sparks in capillary tubes. Exp. Fluids 64, 90.
Rupenthal, I.D, Audghtery, A., 2019. Ocular drugs and drug delivery systems - current trends and futrue perspectives. Drug Discov. Today 28 (8), 1425–1426.
St. Peter, Deidre M, Steger, Jennifer S, Patnaik, Jennifer L, Davis, Nicole, Kahook, Malik Y, Seibold, Leonard K, 2023. Reduction of eyedrop volume for topical ophthalmic medications with the nanodropper bottle adaptor. Med. Devices: Evid. Res. 71–79.
Stachowiak, Jeanne C, von Muhlen, Marcio G, Li, Thomas H, Jalilian, Laleh, Parekh, Sapun H, Fletcher, Daniel A, 2007. Piezoelectric control of needle-free transdermal drug delivery. J. Control. Release 124 (1–2), 88–97.
Sullivan, T.R., Nelson, J., 2010. Combination unit dose dispensing containers. In: US Patent. 7,669,597.
Sultana, Y., Aqil, M., ALi, A., Samad, A., 2007. Advances in the topical ocular drug delivery. Exp. Rev. Ophthamol. 2 (2), 309–323.
Tagawa, Yoshiyuki, Oudalov, Nikolai, Visser, Claas Willem, Peters, Ivo R, van der Meer, Devaraj, Sun, Chao, Prosperetti, Andrea, Lohse, Detlef, 2012. Highly focused supersonic microjets. Phys. Rev. X 2 (3), 031002.
Winfield, A.J., Jessiman, D., Williams, A., Esakowitz, L., 1990. A study of the causes of non-compliance by patients prescribed eyedrops. Br. J. Ophthamol. 74 (8), 477–480.
Yarin, Alexander L., 2006. Drop impact dynamics: splashing, spreading, receding, bouncing.... Annu. Rev. Fluid Mech. 38, 159–192.
Yellepeddi, Venkata Kashyap, Palakurthi, Srinath, 2016. Recent advances in topical ocular drug delivery. J. Ocul. Pharmacol. Ther. 32 (2), 67–82.
Yoon, Ikroh, Shin, Seungwon, 2021. Maximal spreading of droplet during collision on particle: Effects of liquid viscosity and surface curvature. Phys. Fluids 33 (8), 083310.
Zielinski, W.L., Sullivan, T.R., 2007. Ophthalmic drug dleivery - Challenges and advances in Fron-of-they-eye delivery. Drug Deliv. Rep. winter, 44–45.